Supplementary Information

Structure-induced enhancement of thermal conductivities in electrospun polymer nanofibers

Zhenxin Zhong, Matthew C. Wingert, Joe Strzalka, Hsien-Hau Wang, Tao Sun, Jin Wang, Renkun Chen, and Zhang Jiang**

1. E-beam Platinum Bonding Induced Damage

A common method to solve thermal contact issues for suspended nanowire/fiber thermal measurements is to bond the ends of the nanowire or fiber to the heat reservoirs. Often this is accomplished using Pt-C contacts deposited by electron beam via SEM or FIB. This method, however, was found to adversely affect the measurement of the present nylon nanofibers studied. The measured thermal conductivity of fibers was found to decrease after bonding the nanofiber ends with e-beam-deposited Pt-C (Figure S1). This can be explained by way of structural damage induced by either the e-beam exposure or Pt-C deposition, thereby decreasing the fiber thermal conductivity as opposed to reducing the thermal resistance between the nanofiber and thermal reservoirs. Therefore, we elected to measure the nanofibers without the Pt-C deposition. As such, the measured thermal conductivity (κ) reported here represents the lower bound values. Nevertheless, as shown in the next section, the thermal contact resistance is expected to be small compared to the conduction resistance of the nanofibers.

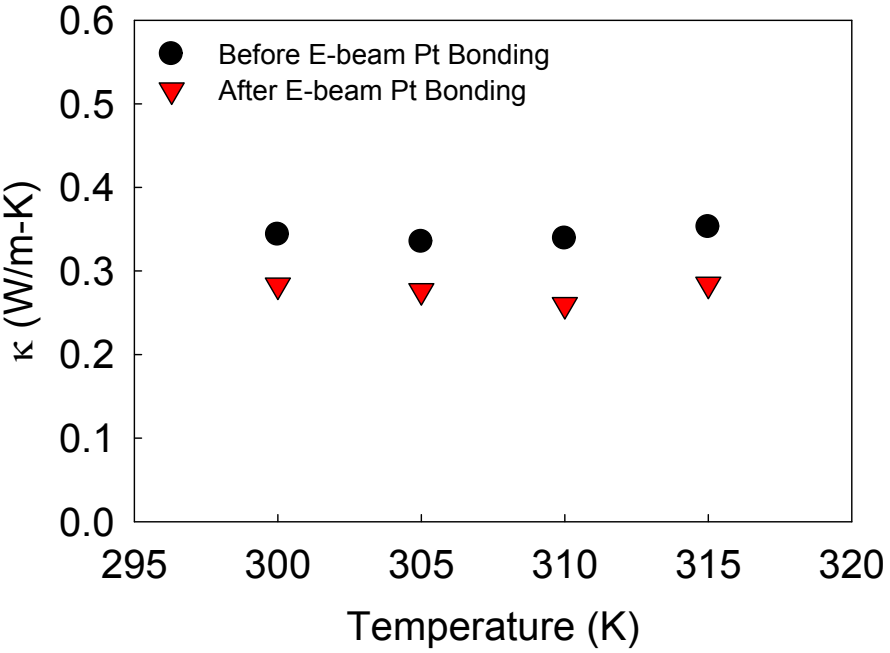

Figure S1: Measured thermal conductivity of a ~400-nm diameter nanofiber before and after e-beam-deposited Pt-C bonding.

2. Estimation of Contact Resistance between Nanofibers and Suspended Pads

Due to the adverse effects of Pt-C deposition, no coating was used for thermal contacts. Therefore, the measured thermal conductivity values represent the lower bound values, which include the thermal contact resistance at the ends of the nanofibers. However, it is important to check the relative importance of this contact resistance in comparison to the overall thermal resistance of the nanofiber. If the fiber resistance is much greater, it would dominate the total thermal resistance, such that contact resistance would not significantly affect our conclusion regarding the diameter dependence of κ.

The thermal contact resistance can be estimated from the constriction resistance of a line contact between the Nylon fiber and the SiN_x pad.[1] The contact width w between a wire and flat surface can be calculated as

$$w = \sqrt{\frac{16F_{vdw}E_m D}{\pi l}}, \quad (1)$$

where D is the fiber diameter, l is the length of fiber in contact with the flat surface, and the effective modulus E_m is

$$E_m = \frac{1}{2}\left[\frac{1-v_s^2}{E_s} + \frac{1-v_p^2}{E_p}\right], \quad (2)$$

where v_s, v_p and E_s, E_p are the Poisson's ratio and Young's modulus of the substrate (SiN_x) and fiber (Nylon), respectively. Furthermore, the van der Waals attractive force F_{vdw} for this geometry is[2]

$$F_{vdw} = \frac{Al\sqrt{D}}{16h^{5/2}}, \quad (3)$$

where the distance between the substrate and wire is h, estimated to be the sum of the van der Waals radii of N, for the SiN_x pad, and H, for the Nylon surface. The Hamaker constant A between SiN_x and Nylon can be estimated to be[3]

$$A = \sqrt{A_{p-p}A_{Si-Si}}, \quad (4)$$

using the Hamaker constants for Si-Si ($A_{Si\text{-}Si}$) and Polystyrene-Polystyrene ($A_{p\text{-}p}$) contacts as a replacement for SiN_x-SiN_x and Nylon-Nylon contacts. The contact resistance between the Nylon fiber and SiN_x pad can be found using

$$R_{cont} = \frac{1}{\pi l k_p}\ln\left(\frac{4D}{w}\right) - \frac{1}{2lk_p} + \frac{1}{\pi l k_s}\ln\left(\frac{2D}{\pi w}\right), \quad (5)$$

where the transverse thermal conductivity of the Nylon fiber k_p is assumed to be the bulk Nylon value of ≈ 0.25 W/m-K; and the SiN_x pad thermal conductivity k_s is ≈ 4 W/m-K; while the total thermal contact resistance for the fiber suspended between two pads is $2R_{cont}$. For fibers of diameter 400 nm and 70 nm, with $l \approx 1$ μm, the contact widths are calculated to be approximately 79 nm and 21 nm, respectively; while the total thermal contact resistance $2R_{cont}$ is roughly 3.8×10^6 K/W and 2.7×10^6 K/W, respectively. This agrees well with experimental studies[4] regarding the thermal contact resistance of carbon nanofibers with suspended devices, which found values of approximately 5×10^6 K/W and had lengths of ≈ 2-3 μm in contact with the suspended pads as opposed to the 20- to 30-μm contact lengths in this study. We can see that these thermal contact resistance values are much less than the thermal resistance due to our nanofiber samples $R_{th} = L/(\kappa A)$, which is estimated to be between 5×10^8 K/W and 3×10^9 K/W, where L and A are the fiber length and cross-sectional area, and κ is the thermal conductivity (assuming 0.3-1.6 W/m-K for fibers with diameters ranging from 70-400 nm). Since the nanofiber resistances are much larger than the contact resistance, they will dominate the measurement.

3. Effects of Heat Loss from Suspended Devices

Using suspended micro-devices to measure the thermal properties of individual nanowires and fibers is a common technique but requires knowledge of the heat currents involved. For devices suspended by long/wide beams, such as those used in this study, heat loss along the length via radiation or conduction by residual gas molecules may not be negligible, and needs to be examined.[5] First, assuming the heat loss from a suspended beam to the ambient is characterized by h, the heat transfer coefficient along the beam, the differential temperature distribution along the suspended beam is

$$\Delta T = \frac{\theta_L \sinh(mx) + \theta_b sinh(m(L-x))}{sinh(mL)}, \tag{6}$$

and the heat current transferred through that beam from the suspending pad to the environment is

$$Q = \sqrt{hPkA}\frac{\theta_b \cosh(mL) - \theta_L}{sinh(mL)}, \tag{7}$$

where P is the perimeter of surfaces undergoing heat loss along the beam, k is the thermal conductivity of the beam, A is the cross sectional area of the beam, L is the length of the beam, $m = \sqrt{hP/(kA)}$, and on the heating pad

$$\theta_L = \begin{cases} \frac{I_h^2 R_b}{hPL}, \ \&heating\ beam \\ 0, \ non-heating\ beam \end{cases} \tag{8}$$

$$\theta_b = \begin{cases} \Delta T_h - \frac{I_h^2 R_b}{hPL}, \ \&heating\ beam \\ \Delta T_h, \ non-heating\ beam \end{cases} \tag{9}$$

while on the sensing pad

$$\theta_L = 0 \tag{10}$$

$$\theta_b = \Delta T_s \tag{11}$$

where ΔT_h is the temperature rise of the heating pad, ΔT_s is the temperature rise of the sensing pad, I_h is the DC heating current applied to the heating pad, and R_b is the resistance of one suspending beam.

Since the total power input to the heating pad ($I_h^2 R_c$) is dissipated through the suspending beams (each with resistance R_b) of both the heating and sensing pads, an energy balance gives us

$$I_h^2 R_c = -4kA\frac{\partial T}{\partial x}\Big|_{\substack{x=0,non-heating,\\ heating\ pad}} - 2kA\frac{\partial T}{\partial x}\Big|_{\substack{x=0,heating,\\ heating\ pad}} - 6kA\frac{\partial T}{\partial x}\Big|_{x=0,\ sensing\ pad}, \quad (12)$$

which becomes

$$I_h^2 R_c = 6\sqrt{hPkA}\coth(mL)\left[\Delta T_h + \Delta T_s\right] - 2I_h^2 R_b \frac{\cosh(mL) - 1}{mL\sinh(mL)}, \quad (13)$$

and can be simplified to

$$I_h^2 R_c + 2fI_h^2 R_b = P_{tot} = G_L\left(\Delta T_h + \Delta T_s\right), \quad (14)$$

where $G_L = 6\sqrt{hPkA}\coth(mL)$ is the total heat loss conductance from the pad, including the heat conduction along the beams and heat loss from the beams to the environment, and f is defined as the heat loss factor

$$f = \frac{\cosh(mL) - 1}{mL\sinh(mL)}. \quad (15)$$

For simplicity, P_{tot} has been defined as the multiplication factor γ multiplied by the power dissipated in the suspended pad ($P_0 = I_h^2 R_c$), namely,

$$P_{tot} = \gamma P_0 = \gamma I_h^2 R_c, \quad (16)$$

and γ is a multiplication factor

$$\gamma = 1 + 2f\frac{R_b}{R_c}. \tag{17}$$

Importantly, *f* represents the fraction of heat generated in the supporting beam that conducts into the suspended pad. When heat loss is negligible, $h \to 0$, the heat loss factor *f* approaches the value 0.5, representing half the heat dissipated in the suspending beams conducting into the heating membrane and the other half conducting to the substrate. In this case, the multiplication factor becomes

$$\gamma = 1 + \frac{R_b}{R_c}, \tag{18}$$

which is the definition used for previous analysis[6] of suspended nanowire measurements with negligible heat loss assumed.

The sensing side measurement requires the use of a Wheatstone bridge circuit, which measures the change in resistance of the suspended pad coil and two of the supporting beams. This leads to a non-uniform temperature distribution, which requires a slight change in the TCR used.[7] That definition, however, is based on the linear temperature distribution in the suspending beams on the sensing side and therefore must also be altered:

$$\Delta R_s = 2\frac{dR_b}{dT}\Delta\bar{T}_b + \frac{dR_c}{dT}\Delta T_p = 2\frac{dR_b}{dT}f\Delta T_p + \frac{dR_c}{dT}\Delta T_p \tag{19}$$

$$TCR_{s,eff} = \left(\frac{dR_s}{dT}\right)_{eff} = \left(\frac{dR_s}{dT}\right)\frac{2fR_b + R_c}{2R_b + R_c} \tag{20}$$

where ΔR_s is the change in resistance of the sensing side including coil and two beams, R_b is the resistance of a single suspending beam, and R_c is the resistance of the coil on the suspended pad.

It is shown from both eqs. (17) and (20) that the heat loss factor f is and important parameter which dictates the degree of heat loss. The heat transfer coefficient, h, has been experimentally measured and was found to be well predicted by radiation heat transfer $h = 4\sigma\varepsilon T^3$, where σ is the Stefan-Boltzmann constant, ε is the emissivity of SiN_x, and T is the absolute temperature of the ambient sample environment.[8] Based on this, we can predict f as function of the ambient temperature according to eq. (15). As shown in Figure S2a, f varies from 0.5 at low temperature to approximately 0.46 at room temperature. Furthermore, definitions of γ and $TCR_{s,eff}$ above can be used to see the effect of heat loss on the system. Heat loss reduces the amount of heat generated in the beam being conducted to the pad and has a larger effect at higher ambient temperatures (Figure S2b), but its overall impact on γ in the studied system is negligible, as shown by the small change in γ (< 1%) from the no heat loss case. The change in the calculated TCR from ideal (no heat loss) conditions is also small (<2% change) (Figure S2c). Since the nanowire sample conductance G_{nw} is calculated from the measured temperature rises of the heating (ΔT_h) and sensing pads (ΔT_s),[6]

$$\Delta T_h = {\Delta R_h}\Big/{\left(\frac{dR_h}{dT}\right)} = \frac{G_L + G_{nw}}{G_L(G_L + 2G_{nw})}\gamma P_0 \quad , \tag{21}$$

$$\Delta T_s = {\Delta R_s}\Big/{\left(\frac{dR_s}{dT}\right)_{eff}} = \frac{G_{nw}}{G_L(G_L + 2G_{nw})}\gamma P_0 \quad , \tag{22}$$

the parameters affected by the heat loss factor each affect the calculated conductance. Since γ and $TCR_{s,eff}$ are not significantly altered, the cumulative effects on the nanowire conductance are themselves limited, as seen in Figure S2(d) (< 1%). Therefore, for the system geometry and

temperature range studied herein, the heat loss along the suspended beams has negligible effect compared to the other uncertainties in the measurement.

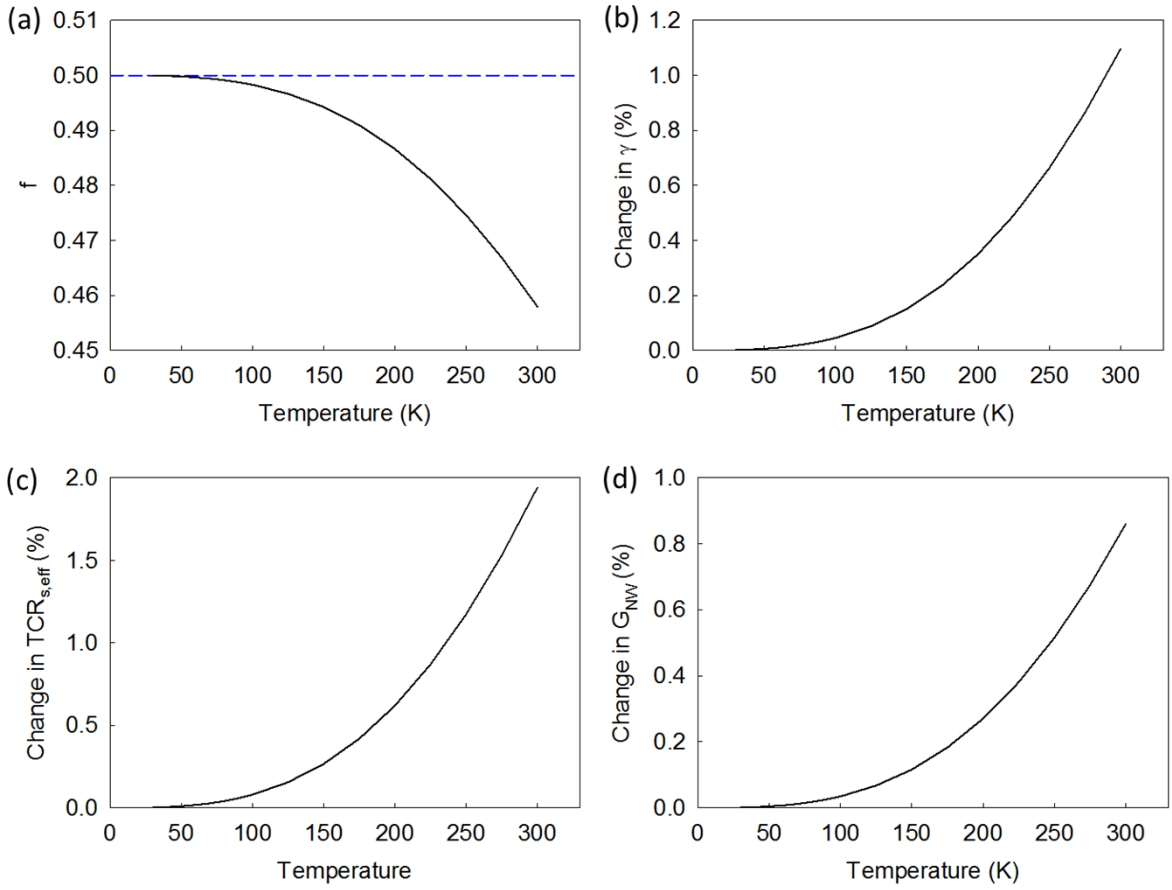

Figure S2: (a) Heat loss factor versus temperature. The upper limit of the heat loss factor is 0.5 for no or negligible heat loss (blue dashed line). (b) Percent change in γ versus temperature. (c) Percent change in $TCR_{s,eff}$ versus temperature. (d) Percent change in calculated nanowire conductance versus temperature. All based on average measured values of device parameters such as beam and coil resistance.

4. Estimation of Heat Loss Along Nanofiber

Since the measured nanofiber samples are long (~20-30 μm) and thermally resistive, radiation or other sources of heat loss along their length could cause measurement errors. To

check if the heat loss has a large effect compared to the heat conducted through the sample, we can look at the ratios of the conduction/heat loss heat rates Q_{loss}/Q_{cond}:

$$Q_{loss} \sim \frac{h\pi DL\Delta T}{2}, \tag{23}$$

$$Q_{cond} = \frac{\kappa\pi D^2\Delta T}{4L}, \tag{24}$$

$$\frac{Q_{loss}}{Q_{cond}} = \frac{2hL^2}{\kappa D}. \tag{25}$$

Here, h is the heat transfer coefficient, calculated to be ~5 W/m^2-K assuming black body behavior (worst case scenario), κ is the nanofiber thermal conductivity, while other constants include fiber diameter D, length L, and temperature difference between the heating and sensing pads ΔT. The heat rate ratios for the largest (413 nm) and smallest (73 nm) nanofibers measured, with lengths of ~20 μm, were ~2.7% and ~3.4%, respectively. This is within the measurement error, and therefore negligible.

5. Diameter Calculation for Beaded Fiber

The effective diameter of the beaded nylon nanofiber was calculated through image processing of the nanofiber profile taken by SEM. The image was treated such that the fiber profile pixels were tagged a specific color using photo-imaging software (ImageJ). Using the pixel scale size in nanometers (from SEM scale bar), the diameters at interval sections along the fiber image (D_i) were calculated. The effective diameter was then found after taking the root of the sum of the squares of the incrementally calculated diameters:

$$D_{eff} = \frac{1}{L}\sqrt{\int_0^L D_i^2 \, dL} \quad . \tag{26}$$

This calculated effective diameter was used to calculate the thermal conductivity of the fiber.

6. Electrospinning and hot-stretching of nanofiber bundles

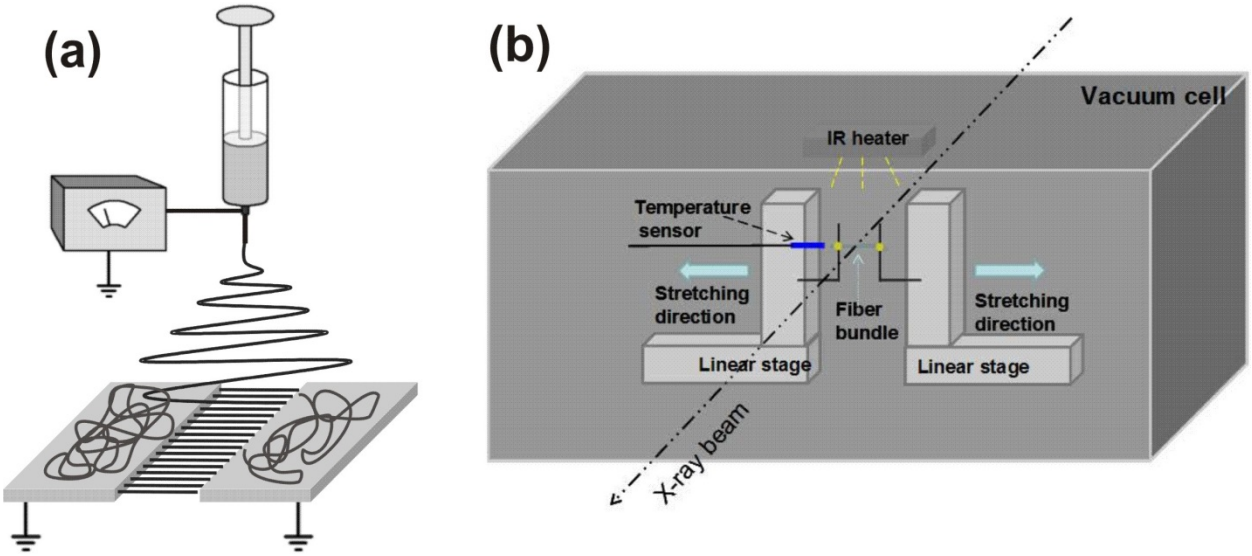

Fig. S3**:** (a) Electrospinning setup. Highly aligned nanofibers are collected on two parallel electrodes. (b) Schematic of the X-ray compatible *in situ* hot-stretching vacuum chamber.

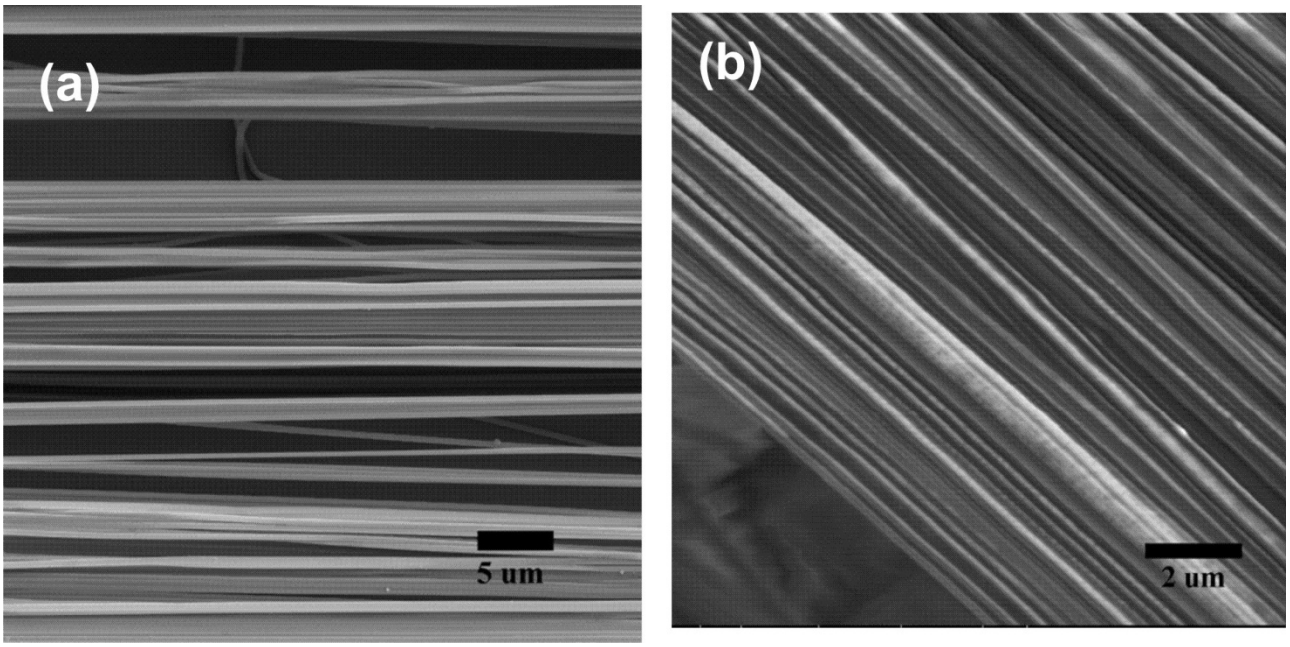

Fig. S4 (a) and (b) are SEM images of aligned fiber bundles (from 10 wt% solution of Nylon-11 in HFIP) before and after hot-stretching, respectively.

7. Calculation and effect of the orientation of fiber alignment

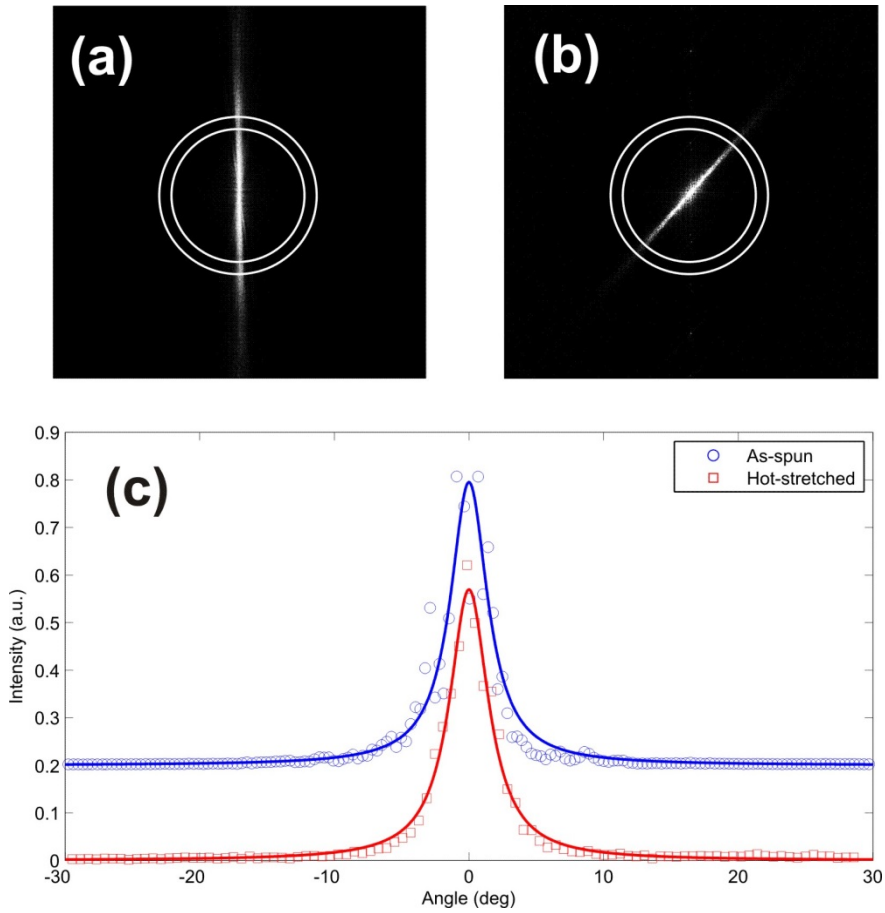

Fig. S5 (a) and (b) are modulus square of the fast Fourier transform of SEM image in Fig. S4. (c) Azimuthal line cuts corresponding to the integrated intensity in the concentric region and their best fit to the model described in the text. For line shape comparison, the data is normalized and shifted vertically.

The apparent values of the average inclination angle of crystalline domains measured in WAXS result from the convolution of the intrinsic inclination angle and the alignment of the fibers with respect to the collection axis. The later can be determined by analyzing SEM images of fiber bundles in the Fourier space. For example, Fig. S5 shows the modulus square of the fast Fourier transform (FFT) of the SEM image in Fig. S4. We use the modulus square because in X-ray experiment the measured intensity is the modulus square of the exit wave field amplitude.

The azimuthal intensity line cuts were analyzed in a similar way as for WAXS data. It was found that the orientational order parameters due to the fiber alignment are $\langle P_2 \rangle_f$=0.955 and 0.954, and the average tilt angles are $\langle \beta \rangle_f$=1.71±0.17 deg and 1.76±0.08 deg for as-spun and hot-stretched fibers, respectively. The fiber alignment is, therefore, preserved during hot-stretching and the orientation improvement obtained from in the WAXS is purely due to the arrangement of the polymer molecules.

For the best orientational distribution achieved in the present, i.e., $\langle P_2 \rangle$=0.86 and $\langle \beta \rangle$=4.7 deg determined from WAXS data analysis on a thin hot-stretched fiber, the intrinsic order parameter is thus given by[9] $\langle P_2 \rangle_c = \langle P_2 \rangle / \langle P_2 \rangle_f$=0.90, and the $\langle \beta \rangle_c = \sqrt{\langle \beta \rangle^2 - \langle \beta \rangle_f^2}$=4.4 deg. Therefore, the effect due to fiber alignment on the WAXS analysis is very small in compared to that due to the intrinsic crystalline arrangement.

8. WAXS from bulk Nylon-11 sample

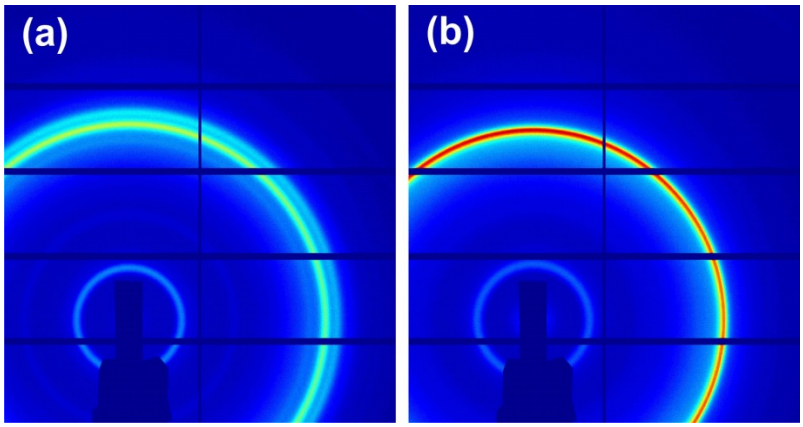

Fig. S6 WAXS patterns from bulk Nylon-11 pellet at (a) RT and (b) 120 °C. The diffraction does not reveal significant orientational preference of the crystallites except that the peak width gets narrower indicating the crystallite size increases.

9. WAXS analysis procedure

The 2D WAXS pattern first undergoes the detector's flat field and solid angle corrections using GIXSGUI, a Sector 8ID/APS beamline data reduction software. The WAXS data analysis for internal structures (Figure 1d-1f) is then performed as follows.

(1) The linecut along the fiber axis, i.e., across (010) peak, is fi9rst performed, which is then modeled by three Lorentzians for the (010) and (020) Bragg diffractions as well as the amorphous scattering. All three peak positions and FWHM (and therefore coherent domain size) are obtained. See Fig. 1d

(2) Perform a narrow linecut along the fiber normal axis, i.e, across (200) peak. With amorphous peak position fixed but its FWHM and scattering weight (intensity) floating, fitting the (200) linecut gives the (200) Bragg peak position and FWHM. See Fig. 1e.

(3) The azimuthal linecut is then performed with a finite q width smaller than the difference of the peak positions of the (200) peak (obtained from step 2) and amorphous peak (obtained from step 1). This minimizes the effect of the amorphous scattering in case of the possibility of preferred orientation of amorphous structures. The azimuthal linecut is then fitted for the crystalline orientational distribution function (ODF) following the procedure described in the paper. From ODF, the 2nd-order orientational order parameter and the average inclination angle of th crystalline domains can be calculated. See Fig. 1f and the paper for details.

10. Crystallinity of the nanofibers

The crystallinity of the fibers is estimated by using a quarter of the WAXS pattern (because of the symmetries of the scattering) and calculating the ratio of the integrated area under the crystalline peaks (200), (010) and (020) to the total integrated intensity. The total scattered angle of the current WAXS pattern is limited so that this analysis can only be viewed as a relative

estimation rather than a precise measurement of the crystallinity. Figure S7 shows the crystallinity of the as-spun fibers as a function of fiber diameter. The crystallinity analysis on the 1.5x drawn fibers is much more challenging because many fibers have been broken towards the end of the drawing, leading to an overall scattering that is much weaker than required for reliable estimation (X-ray air scattering becomes important).

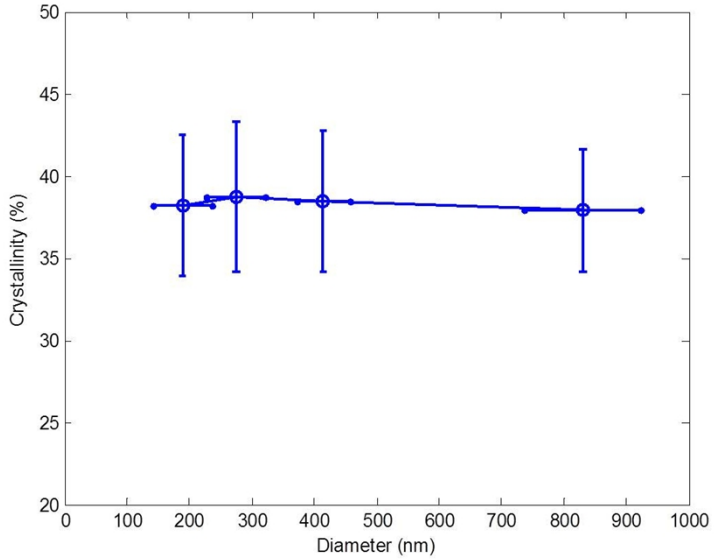

Fig. S7 Crystallinity of as-spun fibers.

References

1. McGee, G. R.; Schankula, M. H.; Yovanovich, M. M. Thermal Resistance of Cylinder-Flat Contacts: Theoretical Analysis and Experimental Verification of a Line-Contact Model. *Nucl Eng Des* 1985, 86, 369-381.
2. Israelachvili, J. N. *Intermolecular and surface forces*. 3rd ed.; Academic Press: Burlington, MA, 2011.
3. Visser, J. Vanderwaals and Other Cohesive Forces Affecting Powder Fluidization. *Powder Technol* 1989, 58, 1-10.
4. Yu, C. H.; Saha, S.; Zhou, J. H.; Shi, L.; Cassell, A. M.; Cruden, B. A.; Ngo, Q.; Li, J. Thermal contact resistance and thermal conductivity of a carbon nanofiber. *J Heat Trans-T Asme* 2006, 128, 234-239.
5. Weathers, A.; Bi, K.; Pettes, M. T.; Shi, L. Reexamination of thermal transport measurements of a low-thermal conductance nanowire with a suspended micro-device. *Review of Scientific Instruments* 2013, 84, 084903.

6. Li, D. Y.; Wu, Y. Y.; Kim, P.; Shi, L.; Yang, P. D.; Majumdar, A. Thermal conductivity of individual silicon nanowires. *Appl Phys Lett* 2003, 83, 2934-2936.
7. Wingert, M. C.; Chen, Z. C. Y.; Kwon, S.; Xiang, J.; Chen, R. K. Ultra-sensitive thermal conductance measurement of one-dimensional nanostructures enhanced by differential bridge. *Review of Scientific Instruments* 2012, 83, 024901.
8. Zheng, J.; Wingert, M. C.; Dechaumphai, E.; Chen, R. Sub-picowatt/kelvin resistive thermometry for probing nanoscale thermal transport. *Review of Scientific Instruments* 2013, 84, 114901.
9. Edwards, M. D.; Mitchell, G. R.; Mohan, S. D; Olley, R. H. Development of orientation during electrospinning of fibres of poly(e-caprolactone). European Polymer Journal 2010, 46, 1175-1183.